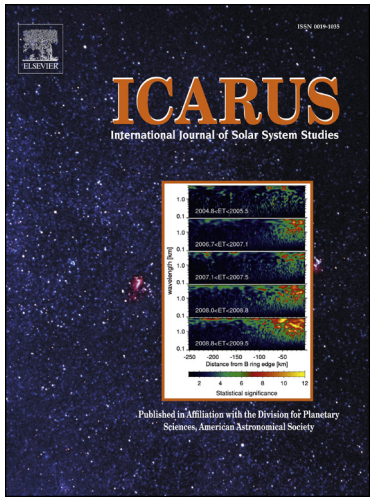

Mapping and characterization of small-scale aeolian structures on Mars: an example from the MSL landing site in Gale Crater

David A. Vaz, Simone Silvestro

PII: S0019-1035(13)00345-X
DOI: http://dx.doi.org/10.1016/j.icarus.2013.08.007
Reference: YICAR 10755

To appear in: *Icarus*

Please cite this article as: Vaz, D.A., Silvestro, S., Mapping and characterization of small-scale aeolian structures on Mars: an example from the MSL landing site in Gale Crater, *Icarus* (2013), doi: http://dx.doi.org/10.1016/j.icarus.2013.08.007

Title

Mapping and characterization of small-scale aeolian structures on Mars: an example from the MSL landing site in Gale Crater

Authors

David A. Vaz[a,b]; Simone Silvestro[c]

Affiliations

[(a)] Centre for Geophysics of the University of Coimbra

vaz.david@gmail.com

Observatório Astronómico da Universidade de Coimbra, Almas de Freire,

3040-004 Coimbra, Portugal

[(b)] CERENA-Centre for Natural Resources and the Environment

Instituto Superior Técnico

Av. Rovisco Pais

1049-001 Lisboa, Portugal

[(c)] Carl Sagan Center, SETI Institute

189 North Bernardo Avenue, Suite 100

Mountain View (CA), 94043, USA

Corresponding author: David Alegre Vaz

vaz.david@gmail.com

Observatório Astronómico da Universidade de Coimbra, Almas de Freire,

3040-004 Coimbra, Portugal

tel.: +351 239 802 370 fax.: +351 239 802 379

Abstract

A new set of methodologies, which allow a simple and fast mapping and characterization of small-scale aeolian structures on Mars is introduced in this work. We follow an object-based approach in which the bedform crestlines are automatically mapped and characterized.

From the methodology validation, we conclude that the quality of the obtained results is comparable with human-produced photointerpretations. We show that the accuracy associated with the measurement of mean trends from the automatically mapped patterns is less than 10º.

Through the analysis of two areas located near the MSL landing site in Gale Crater, we explore some of the possibilities that the automatic mapping technique enables. Namely, for multitemporal surveys and ripple pattern analysis.

We demonstrate how the mapped ripple patterns can be used to assess local wind orientations, and we analyze some examples that illustrate the diversity of wavelength spatial distributions that can be found on Mars. We try to relate these pattern wavelength variations with the possible local influence of granulometry and wind shear velocity.

Highlights

We introduce a set of new tools for analyzing small-scale aeolian bedforms on Mars

We evaluate the accuracy of the new mapping methodologies

Several examples of possible applications are given

Contrasting ripple wavelength spatial distributions are described in Gale Crater

Keywords

Geological processes; Mars, surface; Image processing

1. Introduction

Dune field and ripple patterns, as many natural patterns in nature, are self-organized complex systems (Werner, 1999; Werner and Kocurek, 1999). This means that studying the characteristics of a pattern may shed light on the process that drives its evolution. Many examples of studies using morphometric parameters to characterize the long-term dune field dynamics can be found (Beveridge et al., 2006; Bishop, 2010; Elbelrhiti et al., 2008; Ewing et al., 2006; Kocurek and Ewing, 2005). The classic planimetric discretization of landforms using points or lines is still the preferred methodology, even if it is recognized that it can be a highly subjective task whose results are not necessarily reproducible (Hugenholtz et al., 2012).

The study of subaqueous ripples has profited from the application of objective characterization techniques. By employing sonar data, several workers used spectral analysis (Englert, 2010; Smyth and Li, 2005; Voulgaris and Morin, 2008), the Radon transform (Maier and Hay, 2009) and edge detection techniques (Traykovski, 2007) to retrieve bedforms morphometric parameters (such as wavelength, orientation and height). Skarke and Trembanis (2011) presented and alternative approach, combining the use of local gradients (to obtain wavelengths and orientations) with a defect mapping technique which relies on the identification of the ripple junction points.

The study of Martian wind ripples was recently boosted by the quality and spatial resolution (~ 0.25 m/pixel) of High Resolution Imaging Science Experiment (HiRISE) imagery (Bridges et al., 2007; McEwen et al., 2007). Because sand ripples are influenced by the short term wind flow variability in space and time, their study is fundamental to reconstruct the local wind context of a certain area. To date, the most used pattern characteristics have been the trend and rate of migration of the ripple crestlines, in particular: 1) the trend of the ripple crestlines has been used to reconstruct

the flow pattern over the dunes in Olympia Undae, Arabia Terra, Meridiani Planum and in the Mars Science Laboratory (MSL) landing site in Gale Crater (Ewing et al., 2010; Geissler et al., 2012; Silvestro et al., 2013; Silvestro et al., 2011); 2) the migration rate of the ripple crestlines have been used to provide constraints on sand-moving winds and to calculate sand flux over the Nili Patera sand dunes (Bridges et al., 2012; Silvestro et al., 2010), and the trend and direction of the moving ripple crestlines have been used together to provide a better "ground truth" for testing mesoscale atmospheric wind models in the MSL landing site (Silvestro et al., 2013).

Manually mapping the ripple crestlines has been, to date, the most used technique to derive pattern parameters such as trend and rate of migration (Ewing et al., 2010; Johnson and Zimbelman, 2013; Silvestro et al., 2010). However, this procedure is time consuming and to date only small areas could be analyzed. A first step in using an automatic method for studying ripple populations on Mars has been done by the authors in Arabia Terra and Gale Crater (Silvestro et al., 2013; Silvestro et al., 2011). However, the methodology used in these works has never been properly validated. Here we describe in detail an integrated framework for mapping and analyzing small-scale aeolian ripples from HiRISE data. We will provide the validation of the proposed technique, and we will highlight some of the possible applications, giving special attention to the spatial analysis of ripple patterns.

1.1. Study area

The study area is located ~9 km SW from the Mars Science Laboratory (MSL) Curiosity rover landing site in Gale Crater (Fig. 1). This area is characterized by the presence of dark barchans, dome and linear dunes of basaltic composition (Hobbs et al., 2010; Silvestro et al., 2013). The dunes are predominantly sculpted by two sets of large

ripples (with an average wavelength of 2.7 m) trending 45° and 330°. Both, the dunes and the ripples, show signs of recent activity (Silvestro et al., 2013). In this work, we will focus our attention on the ripple pattern and, in particular, on the methodology used to extract specific morphometric parameters. Due to the complexity of the ripple pattern, the area is ideal for testing our methodology. Regions A and B are analyzed in more detail to illustrate some of the potential offered by the new tools which we are presenting (see section 4.2 and Fig. 1 for location).

FIGURE 1

2. Data and methodology

In this work, we use USGS orthophotos with 0.25 m/pixel resolution (McEwen et al., 2007) and DTMs (digital elevation models) with a spatial resolution of 1m/pixel and a vertical accuracy approaching 20 cm (Kirk et al., 2008). To improve the coregistration between the several images we use, we have defined control points and applied a third order polynomial fit in ArcGIS (a maximum RMSE of 5 cm was achieved). See table 1 for a summary of image characteristics.

As earlier mentioned, spectral analysis and other classic edge detection techniques can be used to estimate the wavelength and orientation of bedforms. A challenge that remote sensing data presents is that bedforms are not uniformly distributed. Ripples are usually clustered and can show a spatial variability of trends and wavelengths, moreover bedrock is frequently exposed. These facts inhibit the use of any methodology that produces global estimates for a given area.

Our approach is to use simple geometric objects (polylines) to map the ripple pattern. The idea is to reproduce the way humans would map the ripple traces in map view, but

doing it automatically and assuring the reproducibility of the results. Putting the problem in this perspective, we take advantage of the lineament mapping techniques first developed for tectonic mapping purposes (Vaz, 2011; Vaz et al., 2012).

On a wider context, the ideas we follow can be included in the field of object-based image analysis (OBIA, or GEOBIA – geographic object-based image analysis) (Blaschke, 2010; Hay and Castilla, 2008; Vaz and Silvestro, 2012). It consists on the application of classic segmentation and classification schemes to obtain higher hierarchy objects. Note that the major difference between our approach and any pixel-based technique is that we can easily merge textural, spectral and multiscale spatial parameters as objects attributes.

On Mars, a two-step algorithm was previously proposed for segmenting and recognizing linear bedforms using MOC (Mars Orbiter Camera) images (Pina et al., 2004). We adopt the same general idea, and we divide the mapping procedure into two main tasks: segmentation of the sand bodies and bedform mapping and characterization (Fig. 2). Using a supervised classification technique, we first assure the segmentation of regions with superimposed bedforms. The obtained mask is then applied after the bedform recognition stage. The final stage corresponds to the vectorization and characterization of the mapped objects.

Through this work, we use several standard morphological image processing operators which for brevity are not defined in detail. The operators are used for textural characterization during the first processing stage, and for generating the ripple marker during the bedform mapping stage. For a formal description and details on the implementation of the operators, readers are referred to Soille (2002).

TABLE 1

FIGURE 2

2.1. Sand bodies segmentation

Despite the albedo differences existent between bedrock and sand bodies, it is not practicable to use a simple threshold to segment the two classes. Shadows in the bedrock areas as well as dune topography produce albedo variations which make the segmentation process more difficult. To overcome these limitations, we adopt a supervised classification technique using artificial neural networks (ANN), a method that is widely used for classifying remote sensing data (Atkinson and Tatnall, 1997; Mas and Flores, 2008; Tso and Mather, 2001).

2.1.1. Texture descriptors

Sand bodies are usually characterized by typical linear textures, differing from more chaotic textures of bedrock areas. Using local texture descriptors also has the advantage of attenuating different illumination conditions. Besides the reflectance values (descriptor d_1), we fed the ANN with several texture descriptors and a topographic normalization matrix computed from the DTM. We use image T1 to train the ANN using the training dataset shown in Fig. 3.

FIGURE 3

To account for reflectance variations due to linear topographies, such as ripples, we use local morphological directional fields computed using line structuring elements (SEs). The descriptor d_2 (Fig. 4b) is defined by $d_2 = f - gdir_\lambda^\gamma(f) + gdir_\lambda^\phi(f)$ where f is the input image, and $gdir_\lambda^\gamma(f)$ and $gdir_\lambda^\phi(f)$ represent the strength of the local

orientation field computed by closing and opening respectively, at scale λ (we use line SEs with 7 pixels).

To enhance the boundaries between the two classes we merge the output of morphological half-gradients. This descriptor (Fig. 4c) is defined according to $d_3 = \rho_B^+(f) - \rho_B^-(f)$ and it is computed from the input image f using an isotropic structuring element B with 5 pixels radius (ρ^+ and ρ^- represent the external and internal morphological gradients).

Another textural descriptor that we use is the local entropy computed on a 6 pixels radius circular neighborhood (Fig. 4d). This descriptor is computed from the local histograms and can be defined according to $d_4 = -\sum_{i=0}^{n-1} p(z_i)\log_2 p(z_i)$, where $p(z_i)$ is the probability of occurrence of a given reflectance value z_i, while n is the number of possible values in the neighborhood (Gonzalez et al., 2004).

We adapt the Minnaert topographic normalization that is commonly applied on remote sensing for removing topographic effects (Blesius and Weirich, 2005; Lu et al., 2008; Walter et al., 2011). The Minneart topographic correction is expressed by $L_H = L_T \cos e/(\cos e \cos i)^k$ with $\cos i = \cos\theta\cos e + \sin\theta\sin e\cos(\varphi_m - \varphi_s)$. L_T is the input reflectance while L_H is the output corrected reflectance. The terrain slope and aspect angles correspond to e and φ_s, while θ and φ_m represent the solar zenith angles and azimuths (Riano et al., 2003).

For simplicity we have not estimated the Minneart exponent k, which would probably assume a different value for each class (Jehl et al., 2008). We used a constant value of $k = 0.1$, but instead of applying the correction to the input image, we used the correction values as one of the inputs for the ANN. We defined this descriptor as

$d_5 = \cos e / (\cos e \cos i)^k$ (Fig. 4e). In this way, we try to reduce the impact of DTM spatial resolution and artifacts in the final classification results.

2.1.2. Training and classification

A pre-processing stage, which consists in the scaling of the input descriptors, is performed. Using the means and standard deviations ($\bar{x}$ and s), the five descriptors are independently scaled from the $[\bar{x} - 2s, \bar{x} + 2s]$ interval to the $[-1,1]$ range (see Fig.4a to e). We use a simple feedforward ANN architecture constituted by one input (with five nodes), one hidden (five nodes) and one output layer (two nodes). We use hyperbolic tangent functions as transfer functions and the training methodology which we employ is the scaled conjugate gradient backpropagation algorithm (Moller, 1993). We obtain a classification overall accuracy of 97% for image T1.

After the classification, the obtained "bedform" class is vectorized and is later used to mask the areas where the bedform mapping technique is applied (Fig. 4f and 5a). See section 4.1 for an example of the application of this same methodology to analyze dune migration.

FIGURE 4

2.2. Bedform mapping and characterization

Bedforms tend to form distinctive linear features where one of the faces will be illuminated and bright, while the other will be shadowed and dark. We explore this linear bright/dark dichotomy to map the bedform traces, focusing on the segmentation of one of the faces, the one that is directly illuminated.

To enhance the brighter linear features on the images we first apply a neighborhood-based morphological contrast enhancement technique defined as $g = [f + \varepsilon_B(gdir_\lambda^\phi(f))]/2$, where f is the input image, ε_B is the erosion operator (B corresponds to a disk SE with a radius of 1 pixel), and $gdir_\lambda^\phi(f)$ is the strength of the local orientation field computed by closing using a SE with 5 pixels. The resultant dataset (Fig. 5b) is then used in the following processing steps.

The marker matrix m is obtained by computing the supremum of the differences between the white top-hats (WTH_{α_i}) and black top-hats (BTH_{α_i}) for all the possible orientations α_i (the length of the line SEs used is 7 pixels) (see Fig. 5c). An hysteresis threshold (aka double threshold, *DBLT*) is used to obtain a binary image, which is then intersected with the bedform marker (bm) obtained with the methodology described in the previous section. These operations are represented by $m = DBLT_{[t_1<t_2<t_{\max}]}\{\vee_{\alpha_i}[WTH_{\alpha_i}(g) - BTH_{\alpha_i}(g)]\} \cap bm$ with $t_1 = 4.2\times10^{-4}$ and $t_2 = 6.7\times10^{-4}$. An example of the obtained results can be seen in Fig. 5d.

The same vectorization methodology described in Vaz (2011) is applied here, producing a lineament database which represent the bedforms traces (Fig. 5e). Several attributes are attached to each object in the database. Geometric parameters, such as length, sinuosity or azimuth (see Fig. 5f for an example of directional segmentation), are computed using geodetic measurements. Summary statistical parameters (minimum, maximum, mean and standard deviation or the mean vector azimuth and circular standard deviation when dealing with angular data) are computed along the objects from a diversity of datasets. For instance, from the original image and derived local orientation fields we obtain textural attributes. From the DTM we derived a full morphometric characterization of the bedforms topographic setting. Besides the

integration of the regional slope and aspect angles we also include longitudinal dips and strikes.

Multitemporal surveys can also benefit from the proposed mapping technique. A minimum bedform displacement value can be simply derived by computing the Euclidean distance between the lines in the two datasets (section 4.1). Finally, the obtained lineament database can be used to produce additional datasets. For instance, the mapped crest lines can be used to derive wavelength estimates (see section 4.3).

3. Bedform mapping accuracy assessment

We have selected three regions, presenting a diversity of bedform geometries, wavelengths and trends, to serve as validation areas for the presented mapping methodology. For each area, we have automatically derived a lineament map (dataset III). Other two datasets (I and II) were obtained through photointerpretation and correspond to the crestlines mapped manually and independently by each author (see Fig. 6 for a detailed view of one of the areas, or Appendix A for a complete view of the compared datasets).

In this section we compare the three datasets both qualitatively and quantitatively. The objective is to validate the results of the described method as well as to give some insight on the possible variability associated with the process of photointerpretation.

FIGURE 6

FIGURE 7

The main differences between the two manually derived datasets (dataset I and II), are located in the areas of intersection of sets of structures with different azimuths (see

the detailed view in Fig. 6). Different topological criteria contribute to the differences in the mapping output, but longer lineaments tend to be equally mapped on both datasets. Dataset III presents the same type of topological discrepancies, it is composed by smaller segments (compare the mean length in Table 2), and generally presents a higher degree of sinuosity since it fits better the local irregularities of the bedform patterns. These characteristics translate in a higher total length of mapped lineaments for dataset III.

In Fig. 7 we show the length-weighted circular distributions for each test area and datasets. The unimodal (Fig. 7a) or bimodal (Figs. 7b, 7c) nature of the distributions is equally well represented in all datasets. The main difference is related with the circular frequencies, with dataset III presenting the lower values. This fact is consistent with the higher circular variances (*V*) associated with dataset III (see Table 2, *V* varies from 0 to 1, with 0 denoting a strong clustering around the mean direction). Also note the different frequencies existent between the two interpreted datasets (I and II) nearby the modal bins (in Fig. 7b for instance).

The absolute frequencies between the datasets can be variable, and are always dependent on the choice of bin size (in this work we use 5º bins on all circular diagrams). Even so, in cases where bimodal distributions are analyzed (Figs. 7b and c) the automatic methodology still allows the relative assessment of each mode magnitude. For the aforementioned cases, the NE-SW set of ripples tends to be predominant, with a stronger asymmetry in Fig. 7c.

On average, a difference of 7.3º exists between the mean azimuth computed for datasets I and II. An average angular difference of 4.8º was obtained between dataset III and I/II. The given values attest that the expectable accuracy for determining the mean

trend of a bedform pattern, either by the traditional or automatic mapping, is always below 10º.

TABLE 2

4. Possible applications

Besides the algorithm validation, we examine some examples of possible applications created by this set of new tools.

4.1. Multitemporal analysis

The described methodology can be used to perform multitemporal monitoring of dune fields. In Figure 8a we show the boundaries of the sand bodies extracted automatically from a sequence of images (T1, T2 and T3) using the same procedure described in section 2.1. It is evident the SW migration of the dune during the analyzed time span. Assuming a bi-orthogonal displacement, a mean displacement of ~2 m was estimated for this upwind edge of the dune, during the T1-T3 time interval. This value of migration matches well with the dune toes advancement calculated for 8 dunes in the same area in a previous work (Silvestro et al., 2013).

Since a true automatic ripple correlation procedure is not yet implemented, we present an example of the minimum migration procedure (Fig. 9). The azimuth of this displacement vectorial field is assumed to be locally orthogonal to the mapped structures. This approach has some limitations: 1) since the bedform correlation is being made between the nearest neighbors, it implies that the measured displacement values are always below half the pattern wavelength; 2) this technique is able to predict the direction of displacement but not the sense of motion of the structures; and 3)

coregistration errors as well as differences in illumination conditions can introduce uncertainties which are not easily quantifiable.

Despite these limitations, the described method could be useful to analyze the spatial distribution of migration rates. For example, in the NE dune the displacements increase toward the dune top. The same dune height/ripple migration relation has been described by Bridges et al. (2012) in Nili Patera. In the SW dune, a similar trend is not evident since in the higher part of the dune the displacement values decrease (dashed area in Fig. 9). This could be interpreted as a clear sign of migration underestimation due to the limitations of the used correlation technique. In that area, the real displacement probably exceeds the threshold value of half the wavelength, which breaks the correlation between the ripples.

To produce results similar to the ones obtained by the application of the COSI-Corr pixel-based tools (Bridges et al., 2012; Necsoiu et al., 2009), we are implementing an object-based cross-correlation which should solve the pointed limitations. The major advantage of our approach, is that we will be able to analyze and relate simultaneously pattern characteristics and migration rates.

FIGURE 8

FIGURE 9

4.2. Characterization of bedform patterns

Ripples are the structures that react faster to wind flow variations, and can be used to access the directions of the predominant winds. At a regional scale, spatial and temporal variations of the ripple main trends have already been analyzed using the described methodologies (Silvestro et al., 2013; Silvestro et al., 2011).

A correlation between bedform wavelength and atmospheric pressure has been studied on Mars (Lorenz et al., 2010), suggesting that wavelength measurements can be used as proxy for wind shear velocity. From fieldwork as well as from numerical and analogue experiments, it is known that the wavelength of a ripple pattern evolves in time (increasing with time until reaching a steady-state regime) and depends on sediment properties (grain size and sorting) and shear velocity (Andreotti et al., 2006; Ouchi and Nishimori, 1995; Pelletier, 2009; Walker, 1981). A linear dependence between wind velocity and ripple wavelength has been described by Andreotti et al. (2006). This relation is expressed by , where λ is the ripple wavelength, is the particle diameter, is the wind shear velocity and is the shear velocity threshold.

Using the proposed methodology, these two parameters (pattern trend and wavelength) can be easily extracted and correlated. Assuming that the wind direction is orthogonal to the ripple crests, it is possible to derive an axial vectorial field that approximates the wind trajectories at the surface. Wavelength is locally estimated by computing the median spacing between the bedforms (bedform orthogonal line segments with 10 m length were used). We have also computed the spacing median absolute deviation (MAD) which gives indication about the variability of the local wavelength. In this way, we obtain a vectorial field ideal for analyzing the spatial distribution of bedform wavelengths.

In the following section, we investigate the possibility of using the wavelength of the ripple pattern as proxy for: 1) the dominant wind direction and 2) wind shear velocity and/or granulometry. The regions A and B (see Fig. 1) are analyzed for this purpose.

4.2.1. Region A

In Fig. 10 we show the estimated wavelengths and median absolute deviation values. The MAD values give us indication about the regularity of the pattern in terms of wavelength (low values mean that the spacing between the ripples is regular, while high MAD values indicate areas where the pattern is less regular). We compare the slipfaces (Fig. 11a shows the stereographic projection of the slipfaces surface vectors) with the mean ripple vectors to evaluate which ripple morphometric parameter (ripple length or wavelength) is able to give a better insight on the long-term wind circulation pattern. In Fig. 11b we show: 1) the classic ripple length-weighted circular distribution, which was rotated by 90º ( ); 2) the mean wavelength vector and 3) the mean λ/MAD ratio vector (see Table 3). We assume that in this case the barchans slipfaces are probably the least unbiased proxies for the regional sediment transport direction and long-term wind circulation pattern.

The wavelength- and λ/MAD-weighted circular distributions show a relative decrease of the NW-SE secondary component visible in the distribution. Both cases produce mean trends which are closer to the slipface axis (<2º difference), while the mean axis is 7.6º degrees apart from that axis. The ripples λ/MAD mean vector has the lower dispersion (with a V= 0.318). These characteristics suggest that the λ/MAD ratio may be a better proxy for inferring regional wind circulation patterns from Martian ripple patterns.

FIGURE 10

FIGURE 11

TABLE 3

The relationship between height and ripple wavelength could also give precious informations about wind shear velocity and grain size distribution. A positive correlation between dune elevation and wavelength is evident in Fig. 10b. The MAD values decrease when moving uphill on the dunes, which means that the pattern becomes more regular in those regions (Fig. 10c).

The linear regression of both variables shown in Fig. 11c seems to be consistent with the expected increasing shear velocity at higher dune heights, as also sustained by the linear correlation between ripple migration and dune height described by Bridges et al. (2012). This means that shear velocity, rather than granulometry, might control the wavelength spatial distribution in this area.

If we assume a constant granulometry, we can try to predict the spatial distribution of wind shear velocities recurring to the direct application of the relation. However, dune grain size segregation is a well known process (Bishop, 2004; Lancaster et al., 2002), which we are not able to spatially constrain in the equation.

4.2.2. Region B

A similar analysis was made for a second area (Fig. 12), revealing a very different arrangement of the ripple pattern. We have a pattern that presents stronger trend bimodality, which is also visible in the λ/MAD-weighted circular distribution (Fig. 13a). A more detailed analysis showed that the NW-SE ripples set is preferentially located in lower dune heights (in Fig. 13b we present the wavelength-weighted circular distribution for the axial vectors located above and below 2 m, note the almost complete absence of the NE-SW component for elevations above 2 m).

In terms of wavelength spatial distribution we observe exactly the opposite of what was found for the two barchan dunes analyzed in the previous example. The higher wavelength values are clustered in the interdune depressions, while the pattern tends to be more regular (lower MAD values) in the higher sections of the dunes (Fig. 12). A negative linear correlation is observed between dune height and wavelength (Fig. 13c).

If in the previous example the positive linear relation seems to support a wind shear controlled wavelength spatial distribution, here we are probably observing a stronger influence of granulometric control (with coarser sediments located in the interdune regions). Field observations made by Lancaster et al. (2002), shown that the spatial distribution of particle size and sorting is not constant in time and space, instead it is highly dependent on the fluctuations of the local wind regime. This means that our interpretation is of course rather simplistic, since we do not know much about particle size distribution, timing and intensity of the wind regime (which in this case is bimodal).

FIGURE 12

FIGURE 13

5. Conclusion

In this work we introduce a set of new tools suited for the integrated analysis of bedform patterns on Mars using HiRISE imagery. The main strength of the proposed framework is that it enables the simultaneous analysis of a large variety of data sources (migration rates and textural or morphometric parameters can now be integrated on a common object/entity).

We have evaluated the accuracy of the automatic methodology and we conclude that the results are consistent with the photointerpretations. From the comparison of two photointerpretations, we suggest that any type of pattern analysis which would be only focused on the pattern topology, is hardly reproducible and would probably produce biased results. The good news is that length-weighted circular statistics produce more stable and comparable results. Besides the bedform mapping, we present several possible applications derived from the core object-based mapping procedure:

1) Multitemporal surveying of dune fields can be easily performed and the local wind circulation patterns can be inferred from the mapped lineaments.

2) Dominant wind directions can be inferred by comparing circular length- and wavelength-weighted statistics with dune morphology. We speculate that the pattern wavelength may be a best proxy for wind direction.

3) It is now possible to evaluate the spatial distribution of the bedforms wavelength over large areas. We analyzed two contrasting cases, where the general spatial arrangement of the ripple pattern seems to be conditioned by the interaction of granulometry and wind shear velocity.

In addition, the data presented, confirm the regional variability of bedform arrangement close to the MSL landing site in Gale Crater. By combining the mapping techniques with new HiRISE images and with the ground observations made by the rover, we expect to generalize and better understand the causes of such variability.

Acknowledgements

We would like to thank the comments and suggestions made by Don Hooper and an anonymous reviewer, and the proofreading made by Nuno Peixinho. This work was

supported by FCT (Fundação para a Ciência e a Tecnologia) with the grant FRH/BPD/72371/2010 and the contracts PEst-OE/CTE/UI0611/2012-CGUC and PTDC/CTE-SPA/117786/2010, with Portuguese and European funds. Simone Silvestro is supported by a grant from the NASA Mars Data Analysis Program (NNH09ZDA001N).

References

Andreotti, B., Claudin, P., Pouliquen, O., 2006. Aeolian sand ripples: Experimental study of fully developed states. Physical Review Letters. 96 (2). Doi 10.1103/Physrevlett.96.028001.

Atkinson, P. M., Tatnall, A. R. L., 1997. Neural networks in remote sensing - Introduction. International Journal of Remote Sensing. 18 (4)**,** 699-709. Doi 10.1080/014311697218700.

Beveridge, C., et al., 2006. Development of spatially diverse and complex dune-field patterns: Gran Desierto Dune Field, Sonora, Mexico. Sedimentology. 53 (6)**,** 1391-1409. Doi 10.1111/j.1365-3091.2006.00814.x.

Bishop, M. A., 2004. A distribution-free statistical method for the spatial characterization of dune granulometry: An example from the Strzelecki Desert, south Australia. Earth Surface Processes and Landforms. 29 (1)**,** 125-131. Doi 10.1002/Esp.1007.

Bishop, M. A., 2010. Nearest neighbor analysis of mega-barchanoid dunes, Ar Rub' al Khali, sand sea: The application of geographical indices to the understanding of dune

field self-organization, maturity and environmental change. Geomorphology. 120 (3-4), 186-194. Doi 10.1016/j.geomorph.2010.03.029.

Blaschke, T., 2010. Object based image analysis for remote sensing. ISPRS Journal of Photogrammetry and Remote Sensing. 65 (1), 2-16. Doi 10.1016/j.isprsjprs.2009.06.004.

Blesius, L., Weirich, F., 2005. The use of the Minnaert correction for land-cover classification in mountainous terrain. International Journal of Remote Sensing. 26 (17), 3831-3851. Doi 10.1080/01431160500104194.

Bridges, N. T., Ayoub, F., Avouac, J. P., Leprince, S., Lucas, A., Mattson, S., 2012. Earth-like sand fluxes on Mars. Nature. 485 (7398), 339-342. Doi 10.1038/Nature11022.

Bridges, N. T., et al., 2007. Windy Mars: A dynamic planet as seen by the HiRISE camera. Geophysical Research Letters. 34 (23). Artn L23205 Doi 10.1029/2007gl031445.

Elbelrhiti, H., Andreotti, B., Claudin, P., 2008. Barchan dune corridors: Field characterization and investigation of control parameters. Journal of Geophysical Research-Earth Surface. 113 (F2). Doi 10.1029/2007jf000767.

Englert, C. M., 2010. Development of spectral analyses for rotary sonar images and comparison to predictive ripple models., Eos. Trans. AGU 91(26) Ocean Sciences Meeting Supplement, Abstract ED25B-13.

Ewing, R. C., Kocurek, G., Lake, L. W., 2006. Pattern analysis of dune-field parameters. Earth Surface Processes and Landforms. 31 (9), 1176-1191. Doi 10.1002/Esp.1312.

Ewing, R. C., Peyret, A.-P. B., Kocurek, G., Bourke, M., 2010. Dune field pattern formation and recent transporting winds in the Olympia Undae Dune Field, north polar region of Mars. Journal of Geophysical Research. 115 (E8), E08005. Doi 10.1029/2009je003526.

Geissler, P. E., Stantzos, N. W., Bridges, N. T., Bourke, M. C., Silvestro, S., Fenton, L. K., 2012. Shifting sands on Mars: insights from tropical intra-crater dunes. Earth Surface Processes and Landforms. 38 (4), 407–412. Doi 10.1002/esp.3331.

Gonzalez, R. C., Woods, R. E., Eddins, S. L., 2004. Digital Image processing using MATLAB. Pearson/Prentice Hall, Upper Saddle River, NJ.

Hay, G. J., Castilla, G., 2008 Geographic Object-Based Image Analysis (GEOBIA): A new name for a new discipline. In: S. L. T. Blaschke, G. J. Hay, (Ed.), Object-Based Image Analysis. Spatial concepts for knowledge-driven remote sensing applications. Springer-Verlag, pp. 75 - 89.

Hobbs, S. W., Paull, D. J., Bourke, M. C., 2010. Aeolian processes and dune morphology in Gale Crater. Icarus. 210 (1), 102-115. Doi 10.1016/j.icarus.2010.06.006.

Hugenholtz, C. H., Levin, N., Barchyn, T. E., Baddock, M. C., 2012. Remote sensing and spatial analysis of aeolian sand dunes: A review and outlook. Earth-Science Reviews. 111 (3-4), 319-334. Doi 10.1016/j.earscirev.2011.11.006.

Jehl, A., et al., 2008. Gusev photometric variability as seen from orbit by HRSC/Mars-express. Icarus. 197 (2), 403-428. Doi 10.1016/j.icarus.2008.05.022.

Johnson, M. B., Zimbelman, J. R., 2013. Characterization of Small Sand Dunes on Mars. 44th Lunar and Planetary Science Conference, The Woodlands, Texas, pp. 2111.

Kirk, R. L., et al., 2008. Ultrahigh resolution topographic mapping of Mars with MRO HiRISE stereo images: Meter-scale slopes of candidate Phoenix landing sites. Journal of Geophysical Research-Planets. 113 (E3). Doi 10.1029/2007JE003000.

Kocurek, G., Ewing, R. C., 2005. Aeolian dune field self-organization - implications for the formation of simple versus complex dune-field patterns. Geomorphology. 72 (1-4), 94-105. Doi 10.1016/j.geomorph.2005.05.005.

Lancaster, N., Nickling, W. G., Neuman, C. M., 2002. Particle size and sorting characteristics of sand in transport on the stoss slope of a small reversing dune. Geomorphology. 43 (3-4), 233-242. Doi 10.1016/S0169-555x(01)00135-0.

Lorenz, R. D., Bridges, N. T., Rosenthal, A. A., 2010. Elevation Dependence of Bedform Wavelength on Tharsis Montes, Mars. Second International Planetary Dunes Workshop: Planetary Analogs -- Integrating Models, Remote Sensing, and Field Data, Vol. LPI Contribution No. 1552, Alamosa, Colorado, pp. 43-44.

Lu, D. S., Ge, H. L., He, S. Z., Xu, A. J., Zhou, G. M., Du, H. Q., 2008. Pixel-based Minnaert Correction Method for Reducing Topographic Effects on a Landsat 7 ETM+ Image. Photogrammetric Engineering and Remote Sensing. 74 (11), 1343-1350.

Maier, I., Hay, A. E., 2009. Occurrence and orientation of anorbital ripples in near-shore sands. Journal of Geophysical Research-Earth Surface. 114. Artn F04022

Doi 10.1029/2008jf001126.

Mas, J. F., Flores, J. J., 2008. The application of artificial neural networks to the analysis of remotely sensed data. International Journal of Remote Sensing. 29 (3), 617-663. Doi 10.1080/01431160701352154.

McEwen, A. S., et al., 2007. Mars Reconnaissance Orbiter's High Resolution Imaging Science Experiment (HiRISE). Journal of Geophysical Research-Planets. 112 (E5). Doi 10.1029/2005je002605.

Moller, M. F., 1993. A Scaled Conjugate-Gradient Algorithm for Fast Supervised Learning. Neural Networks. 6 (4), 525-533. Doi 10.1016/S0893-6080(05)80056-5.

Necsoiu, M., Leprince, S., Hooper, D. M., Dinwiddie, C. L., McGinnis, R. N., Walter, G. R., 2009. Monitoring migration rates of an active subarctic dune field using optical imagery. Remote Sensing of Environment. 113 (11), 2441-2447. Doi 10.1016/j.rse.2009.07.004.

Ouchi, N. B., Nishimori, H., 1995. Modeling of wind-blown sand using cellular automata. Physical Review E. 52 (6), 5877-5880. Doi 10.1103/PhysRevE.52.5877.

Pelletier, J. D., 2009. Controls on the height and spacing of eolian ripples and transverse dunes: A numerical modeling investigation. Geomorphology. 105 (3-4), 322-333. Doi 10.1016/j.geomorph.2008.10.010.

Pina, P., Saraiva, J., Barata, T., 2004. Automatic recognition of aeolian ripples on Mars. XXXV Lunar and Planetary Science Conference, abstract 1621, League City.

Riano, D., Chuvieco, E., Salas, J., Aguado, I., 2003. Assessment of different topographic corrections in Landsat-TM data for mapping vegetation types. IEEE

Transactions on Geoscience and Remote Sensing. 41 (5), 1056-1061. Doi 10.1109/Tgrs.2003.811693.

Silvestro, S., Fenton, L. K., Vaz, D. A., Bridges, N. T., Ori, G. G., 2010. Ripple migration and dune activity on Mars: Evidence for dynamic wind processes. Geophysical Research Letters. 37 (20), L20203. Doi 10.1029/2010gl044743.

Silvestro, S., et al., 2013. Pervasive aeolian activity along Curiosity's traverse in Gale Crater, Mars. Geology. 41 (4), 483-486 Doi 10.1130/G34162.1.

Silvestro, S., Vaz, D. A., Fenton, L. K., Geissler, P. E., 2011. Active aeolian processes on Mars: A regional study in Arabia and Meridiani Terrae. Geophysical Research Letters. 38 (20), L20201. Doi 10.1029/2011gl048955.

Skarke, A., Trembanis, A. C., 2011. Parameterization of bedform morphology and defect density with fingerprint analysis techniques. Continental Shelf Research. 31 (16), 1688-1700. Doi 10.1016/j.csr.2011.07.009.

Smyth, C. E., Li, M. Z., 2005. Wave-current bedform scales, orientation, and migration on Sable Island Bank. Journal of Geophysical Research-Oceans. 110 (C2). Doi 10.1029/2004JC002569.

Soille, P., 2002. Morphological Image Analysis - Principles and Applications. Springer-Verlag, Berlin.

Traykovski, P., 2007. Observations of wave orbital scale ripples and a nonequilibrium time-dependent model. Journal of Geophysical Research-Oceans. 112 (C6). Doi 10.1029/2006jc003811.

Tso, B., Mather, P. M., 2001. Classification methods for remotely sensed data. Taylor & Francis, New York.

Vaz, D. A., 2011. Analysis of a Thaumasia Planum rift through automatic mapping and strain characterization of normal faults. Planetary and Space Science. 59 (11-12), 1210-1221. Doi 10.1016/j.pss.2010.07.008.

Vaz, D. A., Di Achille, G., Barata, M. T., Alves, E. I., 2012. Tectonic lineament mapping of the Thaumasia Plateau, Mars: Comparing results from photointerpretation and a semi-automatic approach. Computers & Geosciences. 48 (0), 162-172. DOI:10.1016/j.cageo.2012.05.008.

Vaz, D. A., Silvestro, S., 2012. An object based approach for the mapping and characterization of Mars ripples. The Third International Planetary Dunes Workshop: Remote Sensing and Image Analysis of Planetary Dunes, Vol. Abs #7019, Flagstaff, AZ, USA.

Voulgaris, G., Morin, J. P., 2008. A long-term real time sea bed morphology evolution system in the South Atlantic Bight. Proceedings of the IEEE/OES/CMTC Ninth Working Conference on Current Measurement Technology. 71-79.

Walker, J. D., 1981. An experimental study of wind ripples. Massachusetts Institute of Technology. Dept. of Earth and Planetary Sciences., Vol. M.S. Thesis. Massachusetts Institute of Technology, Cambridge, pp. 145.

Walter, S., Kirk, R., McGuire, P. C., Neukum, G., 2011. HRSC Topographic Correction by Minnaert Photometric Modeling. EPSC-DPS Joint Meeting 2011, Nantes, pp. 648.

Werner, B. T., 1999. Complexity in Natural Landform Patterns. Science. 284 (5411), 102–104. Doi:10.1126/science.284.5411.102.

Werner, B. T., Kocurek, G., 1999. Bedform spacing from defect dynamics. Geology. 27 (8), 727-730. Doi 10.1130/0091-7613(1999)027<0727:Bsfdd>2.3.Co;2.

Tables

Table 1 – List of images used in this work. T2 image is used for all the pattern characterization tasks, while for multitemporal survey purposes we use all the images.

ID	Image	Ls	Date of acquisition
T1	PSP_001488_1750_RED_A_01_ORTHO	138.17	2006-11-20
T2	PSP_009650_1755_RED_A_01_ORTHO	113.93	2008-08-17
T3	ESP_024234_1755_RED_A_01_ORTHO	7.03	2011-09-27

Table 2 – Summary statistics for the three compared areas (Appendix A Figs. a, e and i) and datasets (datasets I and II correspond to the two photointerpretations, while dataset III was obtained automatically). The mean vector azimuth ($\bar{c}$), circular variance (V), circular standard deviation (v), mean length ($\bar{L}$), length standard deviation (s_L) and total length ($\sum L$) are the presented parameters. See text for discussion.

Area	Dataset	$\bar{c}$	V	v	$\bar{L}$	s_L	$\sum L$
1	I	27.6	0.3	51.3	6.2	5.0	4643.5
	II	23.3	0.2	42.9	6.2	5.9	4544.7
	III	24.1	0.5	63.8	5.2	4.7	6288.9
2	I	22.2	0.8	96.4	6.0	5.0	5274.3
	II	7.1	0.8	99.4	6.1	5.2	6178.3
	III	14.9	0.7	91.6	5.0	4.2	6495.2
3	I	50.1	0.6	75.6	5.9	5.3	4702.4
	II	52.6	0.6	73.2	5.6	6.2	4459.5
	III	46.6	0.7	84.1	5.1	4.4	5116.8

Table 3 – Mean axial trends comparison for the classic ripple length-weighted circular distribution rotated by 90º (L_{90}), the mean wavelength vector (λ), the λ/MAD ratio mean vector and the mean vector computed from the slipfaces slope and aspect angles. Mean azimuth ($\bar{c}$) and circular variance (V) are the presented parameters.

	$\bar{c}$	V
L_{90}	74.2	0.628
λ	67.0	0.346
λ/MAD	65.3	0.318
Slipfaces axis (mean vector strike and dip)	66.6 (N246.6ºW; 28.4SW)	0.013

Figure captions

Figure 1 – The two study areas located on Gale Crater which are used to illustrate the application of the proposed set of methodologies (CTX mosaic).

Figure 2 – Methodology diagram with the main processing steps necessary to automatically extract the bedform patterns from HIRISE imagery.

Figure 3 – Training dataset used as input to the neural network classifier in order to obtain a bedform mask (see Fig. 1 for location, region A). We preferentially include the dune edges areas, and we try to include profiles over the dunes with several orientations, so that the variations in albedo due to dune topography are well represented in the training dataset.

Figure 4 – Texture descriptors used in the segmentation of the bedforms (see text for details): a) descriptor d_1 (input image T1); b) descriptor d_2; c) descriptor d_3; d) descriptor d_4 (local entropy); e) descriptor d_5 (topographic correction descriptor); f) boundary between the two classes.

Figure 5 – Example of bedform mapping: a) input image and mapping mask boundary; b) morphological contrast enhancement; c) bedform marker; d) binary

bedform marker; e) vectorized bedform traces; f) example of directional segmentation of the mapped lineaments, note the existence and overlap of two sets of ripples.

Figure 6 – Detailed view of the three datasets (see Appendix A for a complete view). The main difference between the manually mapped patterns (datasets I and II) is related with different topological criteria (note how the same feature can be mapped using longer or shorter line segments). Dataset III presents a higher degree of sinuosity since the bedforms are traced with more detail. a) input image; b) dataset I; c) dataset II; d) dataset III.

Figure 7 – Length-weighted circular distributions obtained from the automatically mapped dataset (dataset III) and from two photointerpretations made independently by each author (datasets I and II) on three different areas (see Appendix A). Notice the general agreement between the location of the modal trends in all datasets, and the different relative frequencies (see table 2 for the summary circular statistics).

Figure 8 – Example of the application of the segmentation technique for analyzing the migration of a dune during the T1 – T3 time interval: a) mapped dune boundaries; b) mean migration vector computed assuming a bi-orthogonal migration between the T1 and T3 boundary traces.

Figure 9 – Minimum migration axial field computed for the T1-T2 interval. The dashed area indicates a region where the ripple migration exceeds the half wavelength threshold, which produces an artificial decrease of the migration values.

Figure 10 – Wavelength spatial distribution. a) dune elevation; b) wavelength axial vectorial field; c) median absolute deviation (MAD) derived from the wavelength estimation process. The higher wavelengths and lower MAD values are centered in the higher elevation (see Fig. 11c).

Figure 11 –Analysis of the wavelength vectorial field displayed in Fig. 10. a) stereographic projection of the slipface surfaces (the slope and aspect angles derived from the DTM where used to produce this diagram); b) comparison of the ripple length-weighted spatial distribution L_{90^o} (which was rotated by 90º so that it should approximate the wind regime responsible for ripple formation) with the wavelength- (λ) and λ/MAD ratio-weighted spatial distributions; c) linear regression of dune elevation and ripple wavelength.

Figure 12 - Wavelength spatial distribution (see Fig. 1 for location, area B). a) HIRISE image; b) dune elevation; c) wavelength axial vectorial field; d) median absolute deviation (MAD) derived from the wavelength estimation process. Note the clustering of lower wavelength MAD values in the higher sections of the dunes (see Fig. 13c).

Figure 13 - Analysis of the wavelength vectors displayed in Fig. 12. a) comparison of the ripple length, wavelength- (λ) and λ/MAD-weighted spatial distribution; b) height segmented circular distribution of the wavelength parameter for dune elevations below and above 2 m ($\lambda_{H<2}$ and $\lambda_{H>=2}$); c) linear regression of dune elevation and ripples wavelength.

Appendix A

A1 – Complete view of the datasets used for validation. Each row corresponds to one of the analyzed regions (respectively 1, 2 and 3). The second, third and fourth columns show the mapped crestlines on each dataset (I, II and III). Refer to Fig. 7 and Table 2 for the derived circular diagrams and statistics.

APPENDIX A

Figure 1

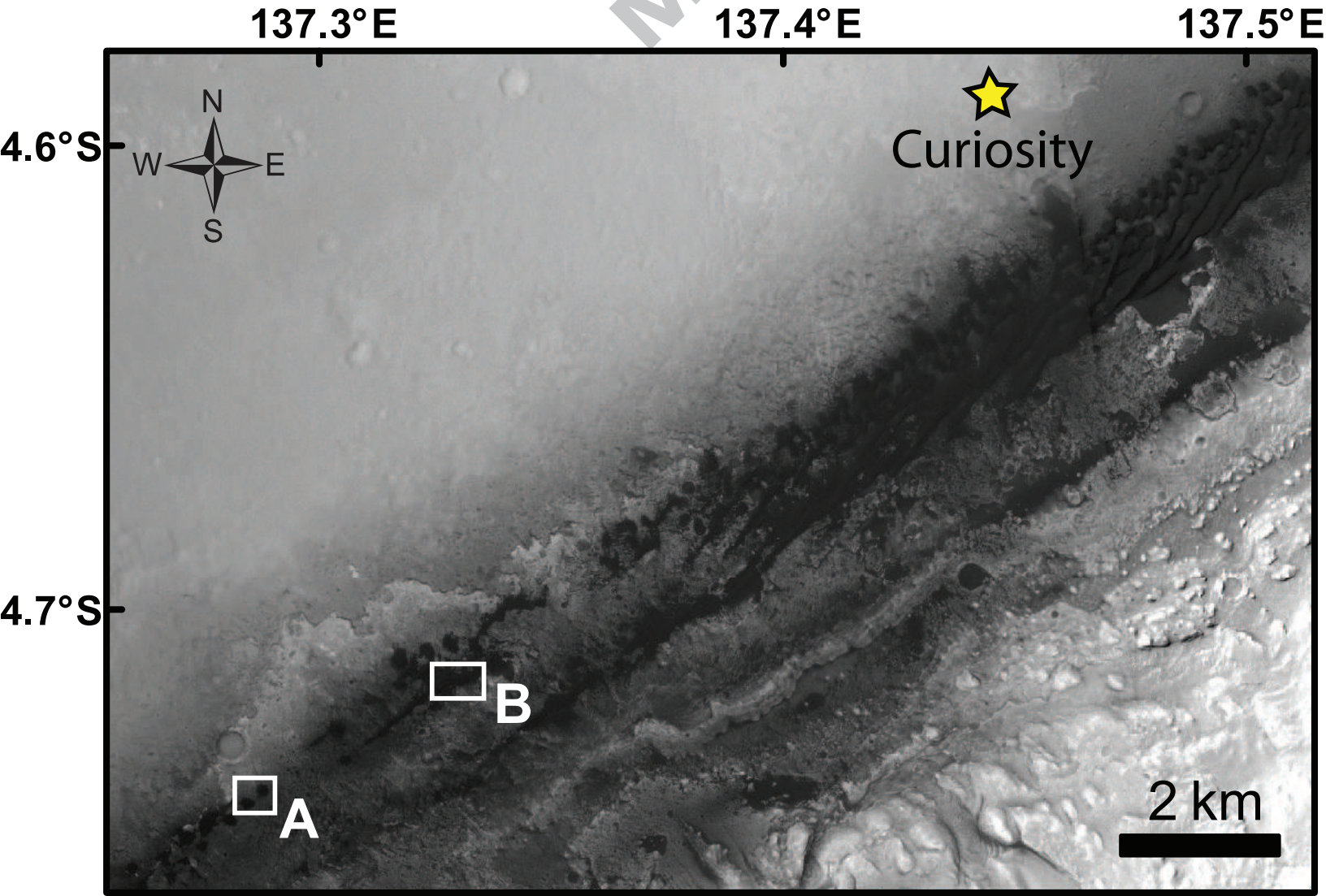

Figure 2

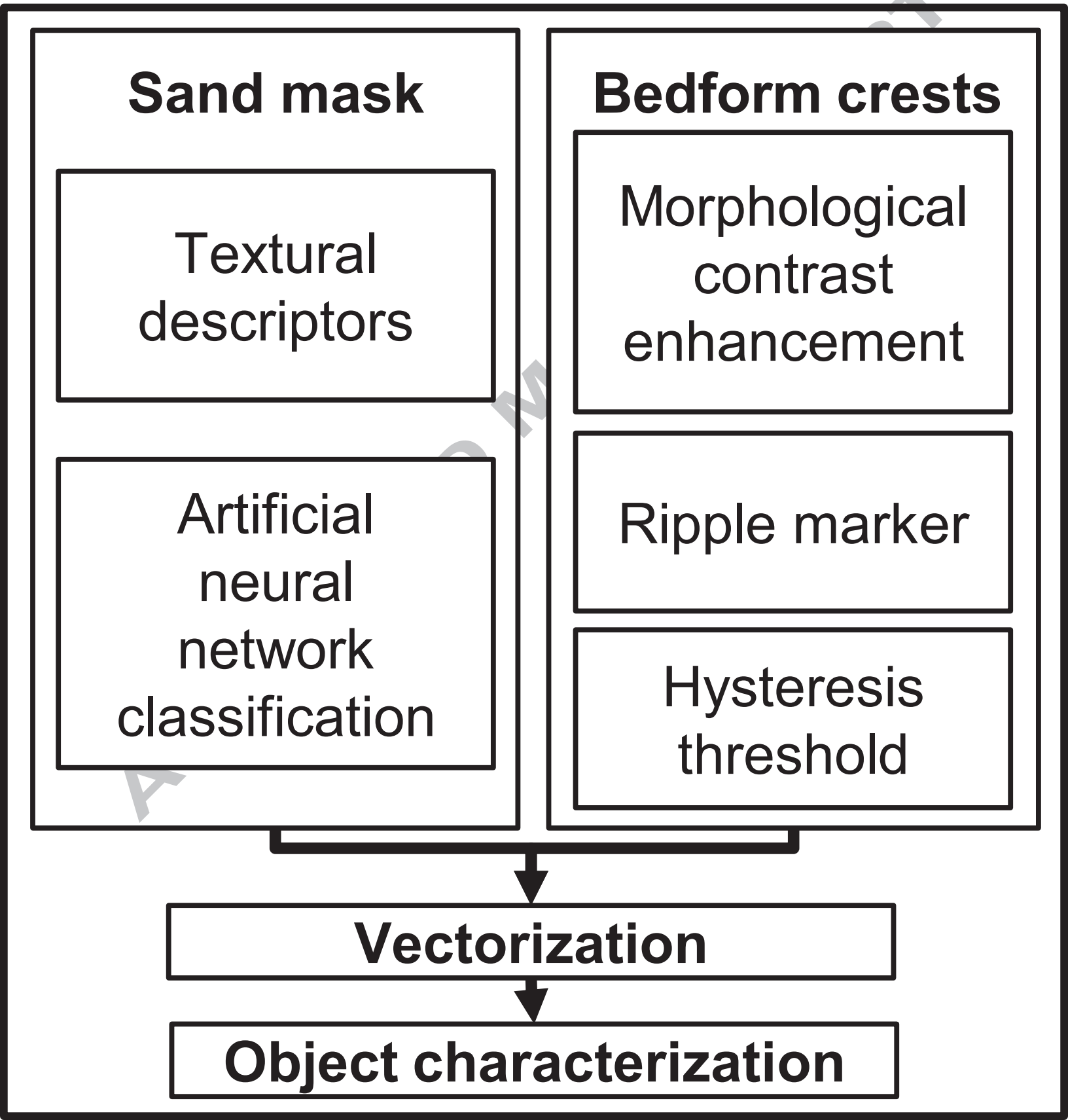

Figure 3

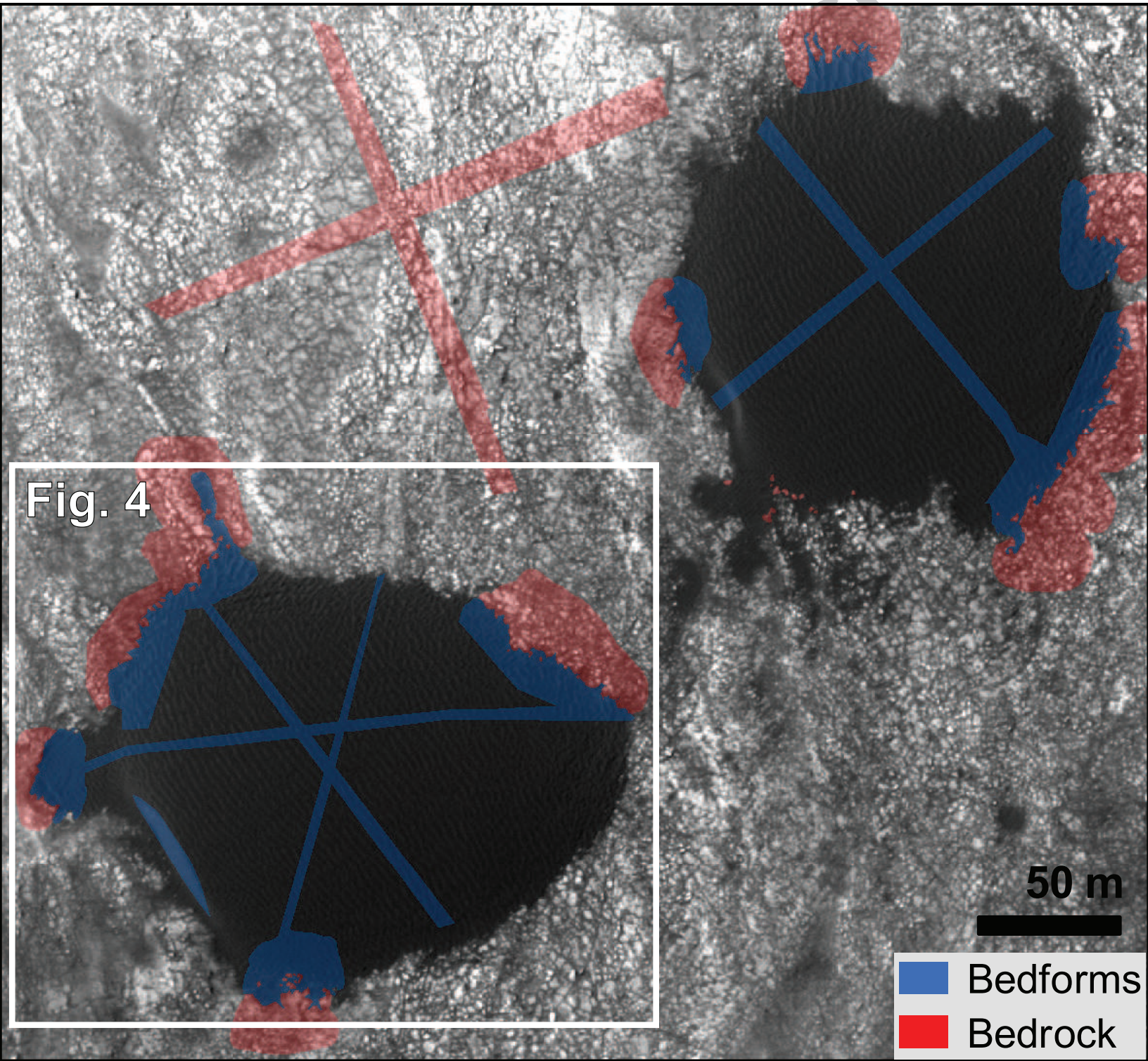

Figure 4

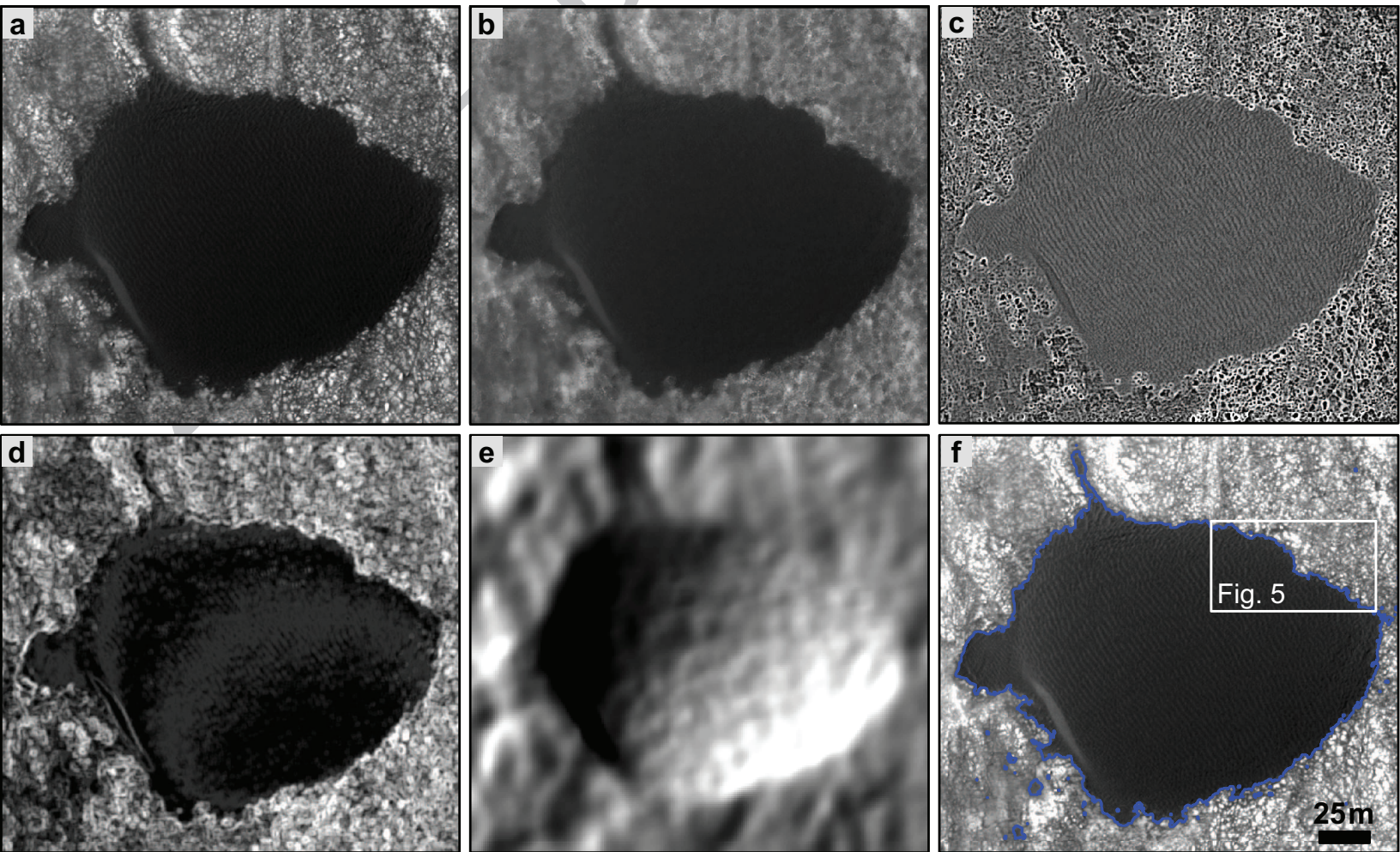

Figure 5

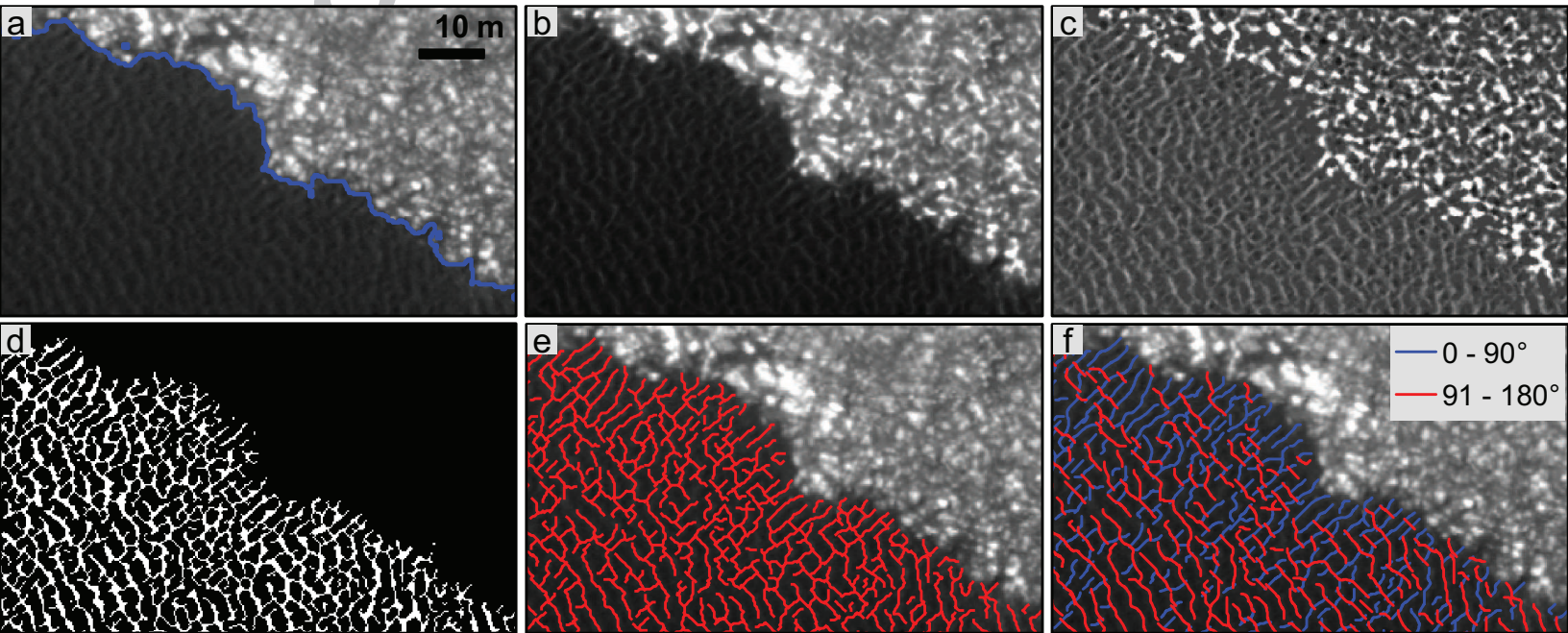

Figure 6

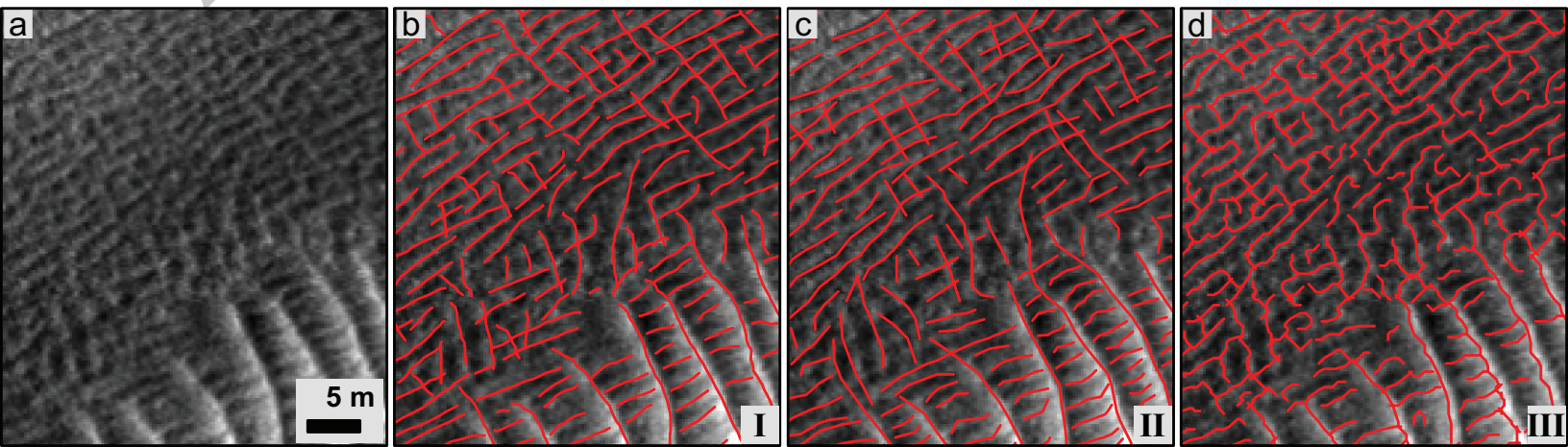

Figure 7

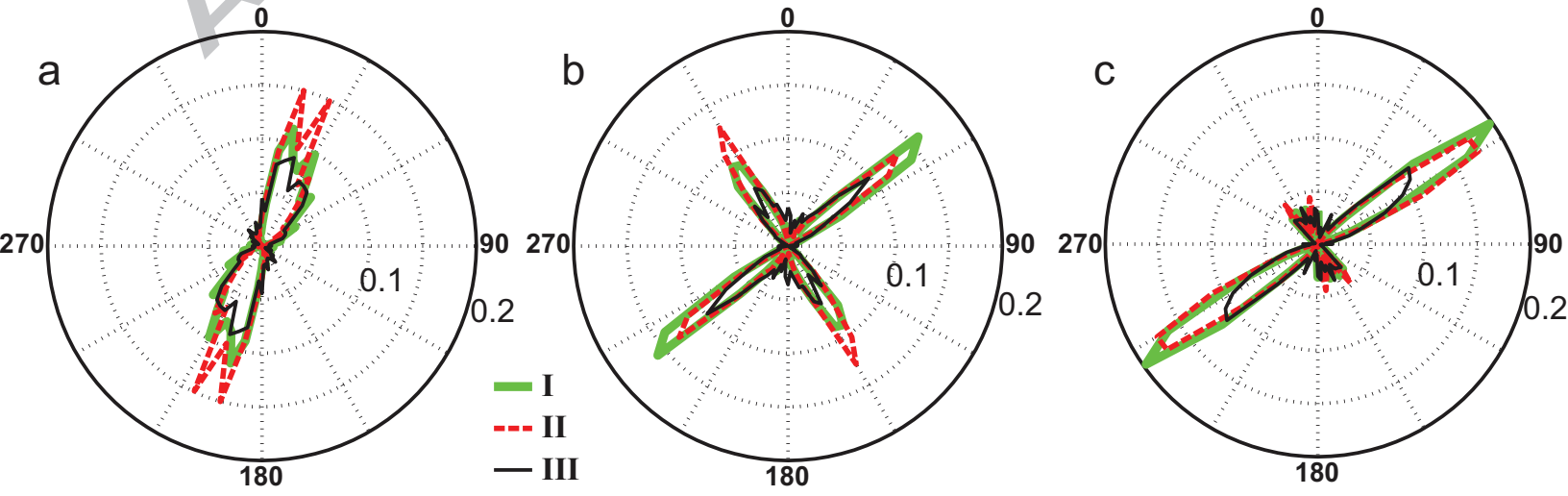

Figure 8

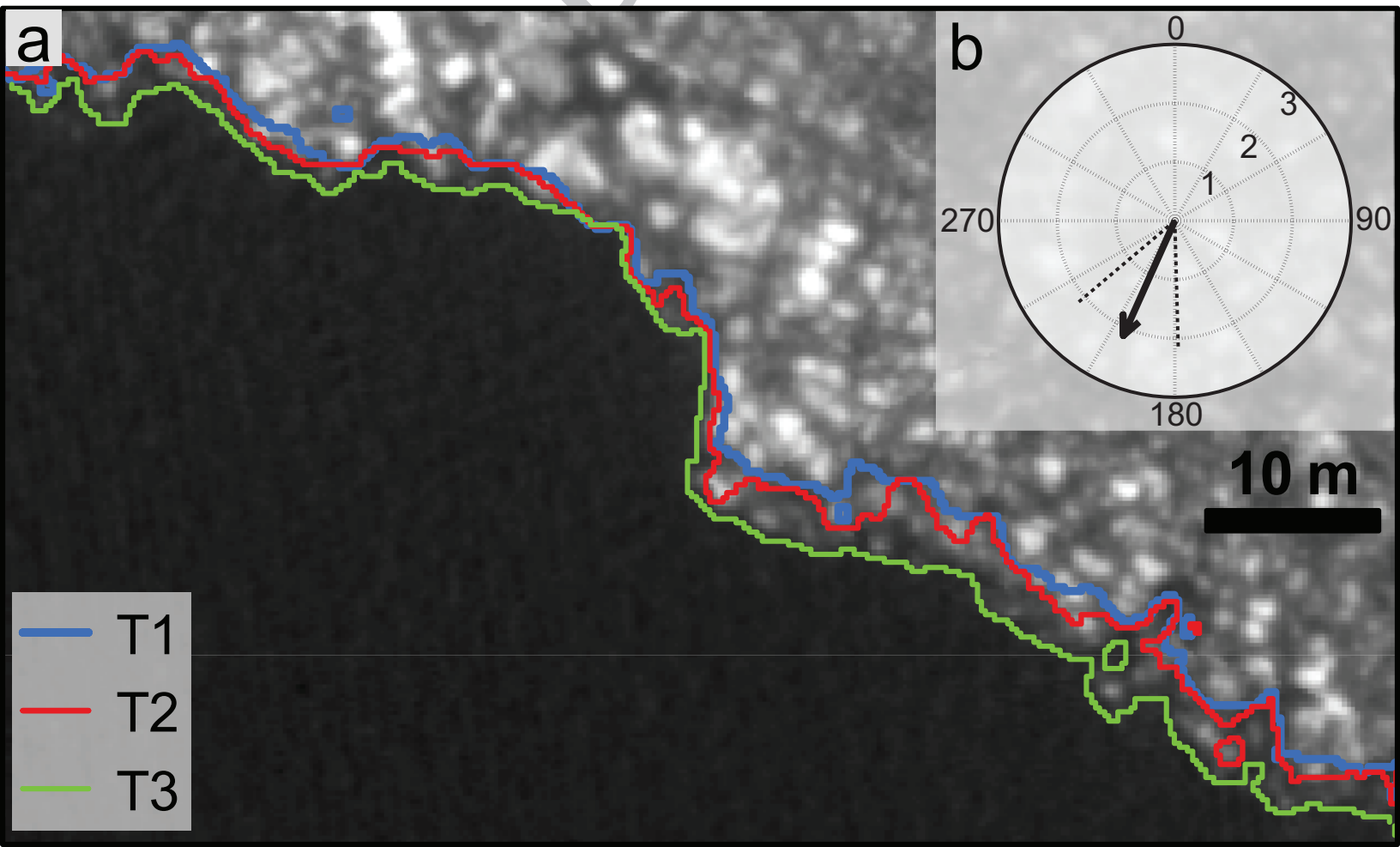

Figure 9

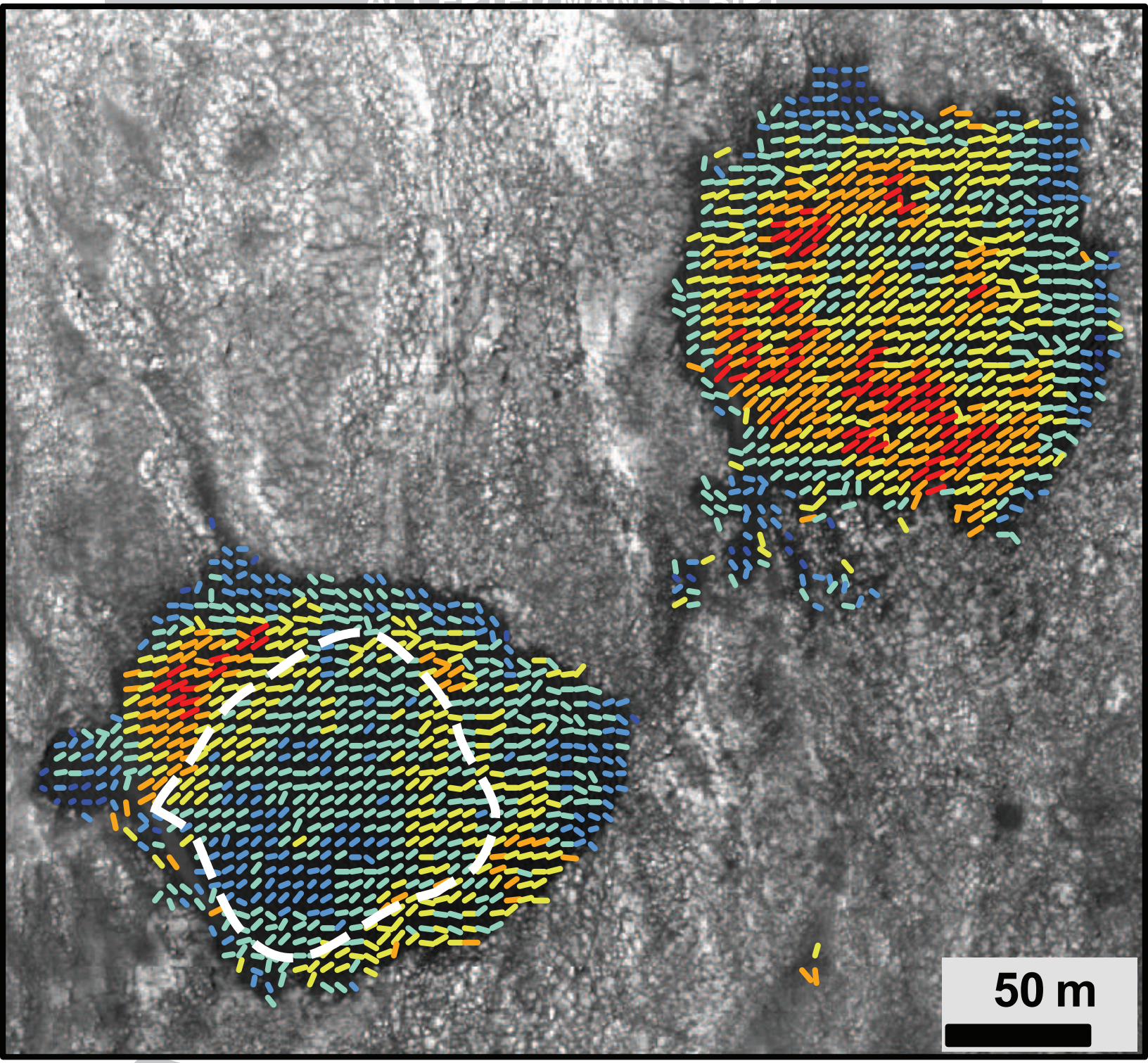

Minimum migration (m)

0.08 - 0.25
0.26 - 0.35
0.36 - 0.45
0.46 - 0.55
0.56 - 0.65
0.66 - 0.83

Figure 10

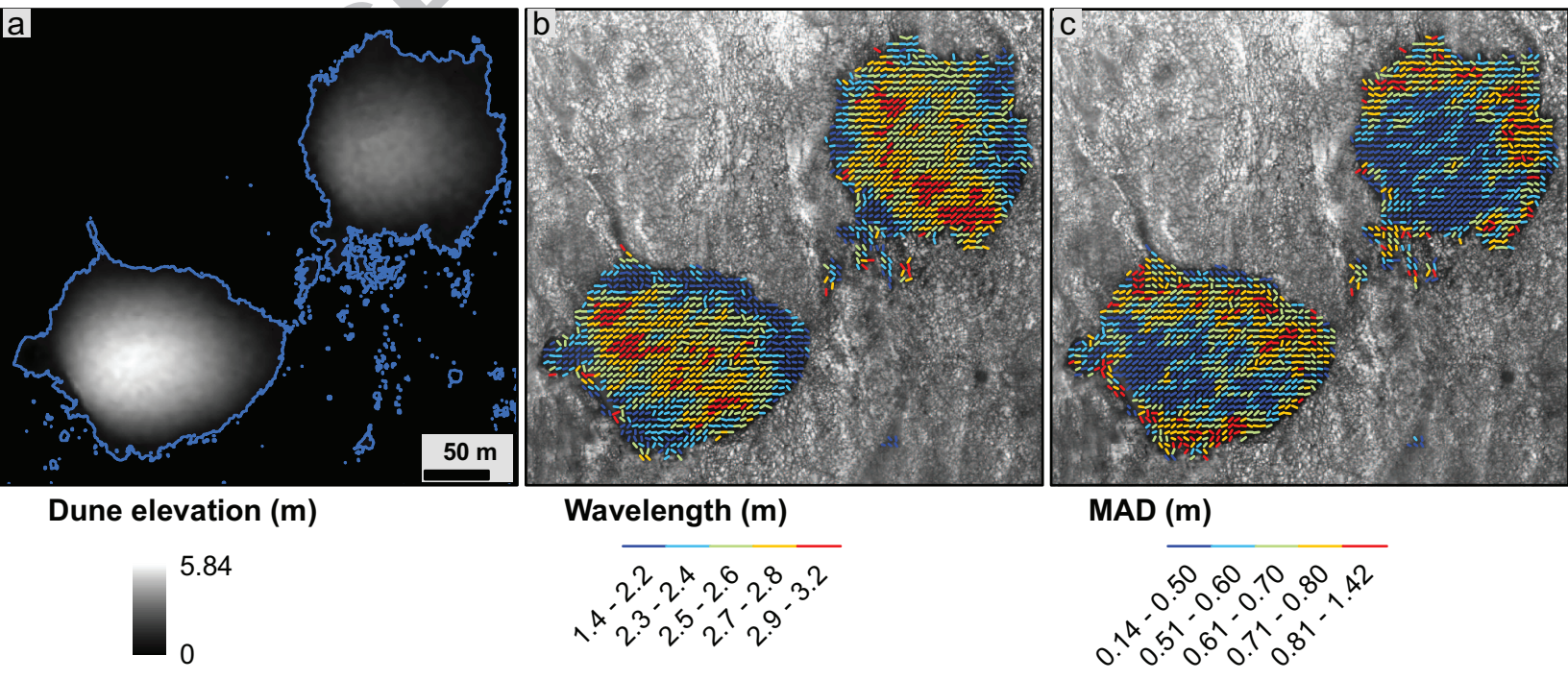

Figure 11

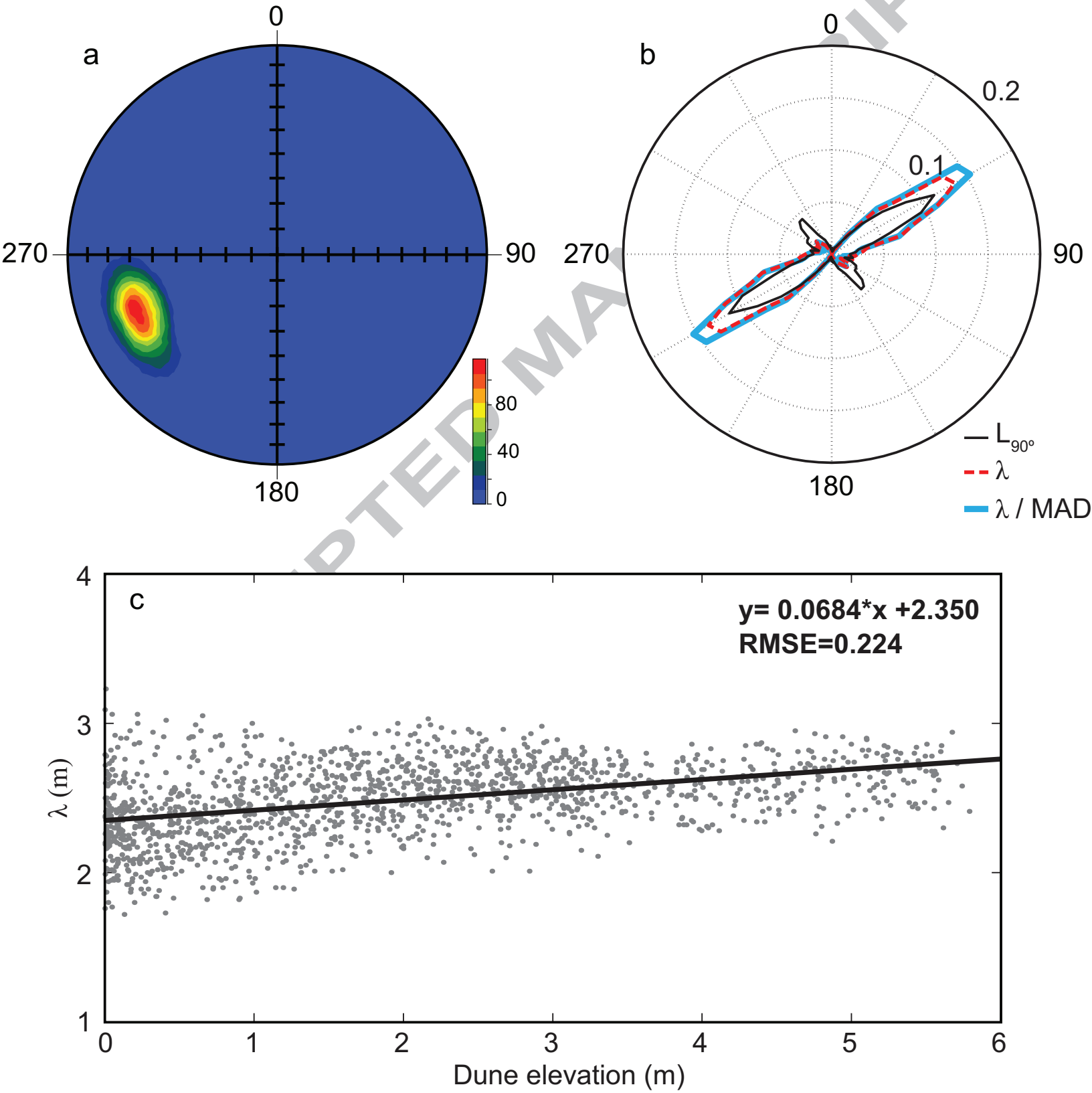

Figure 12

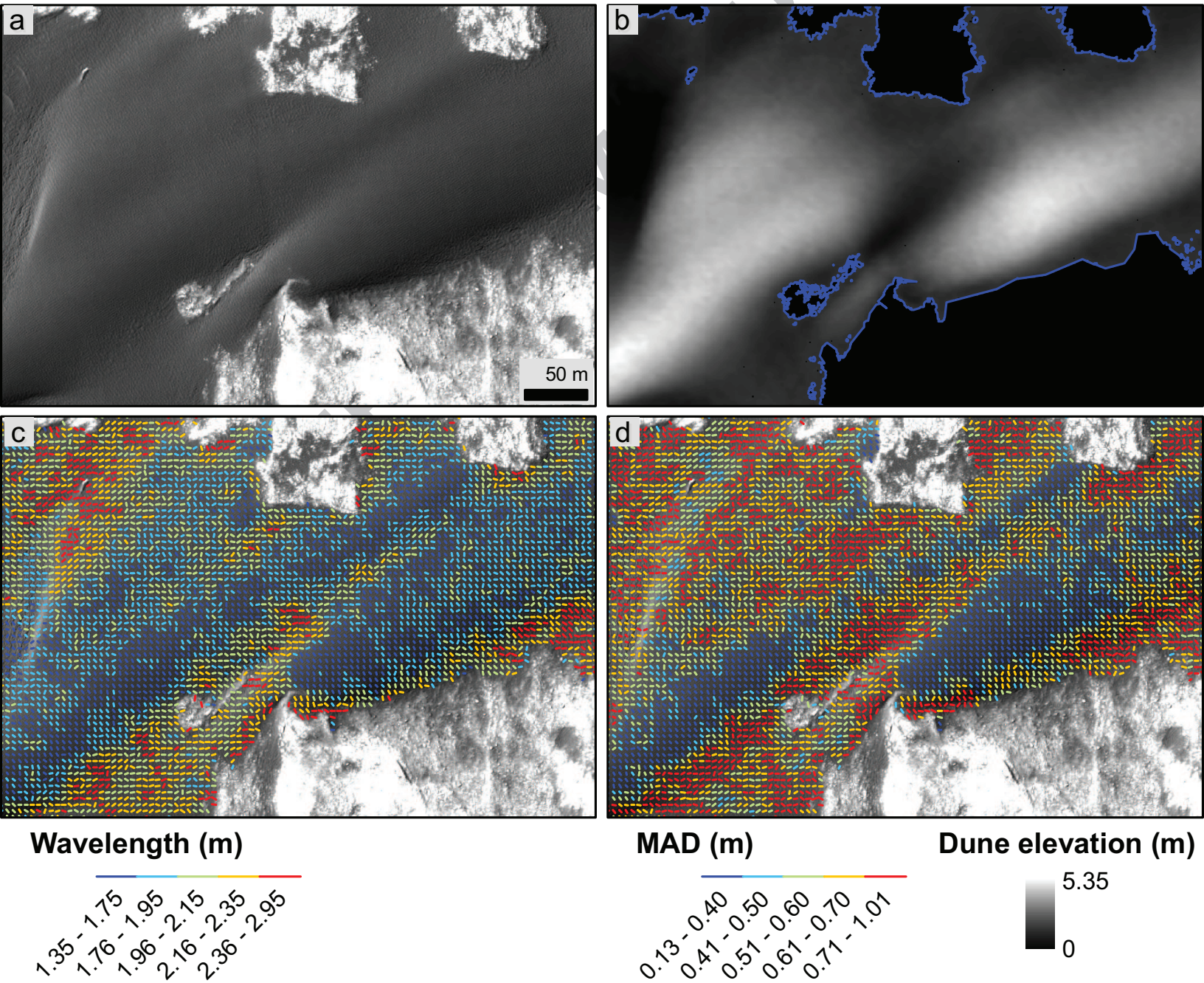

Figure 13

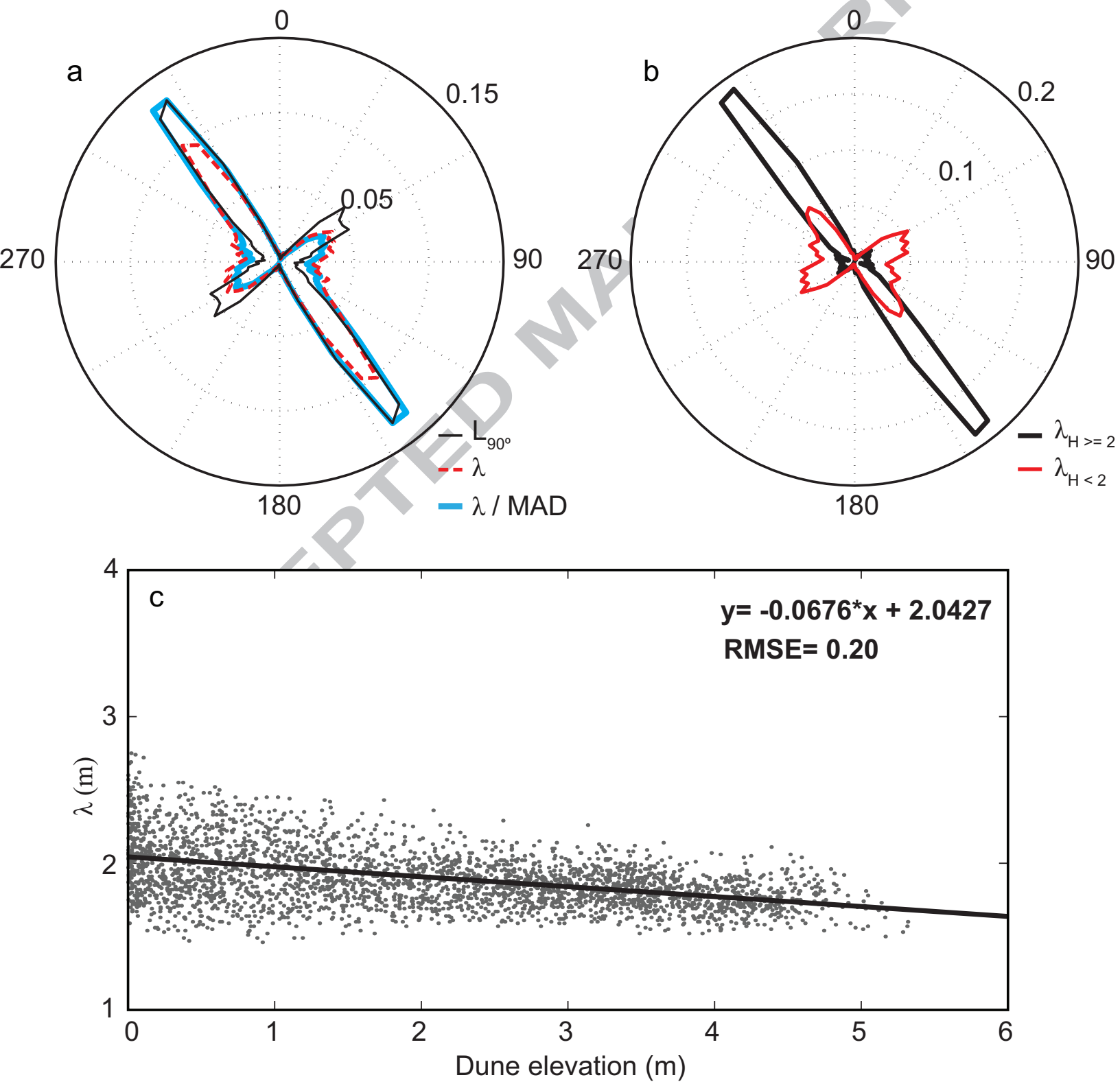

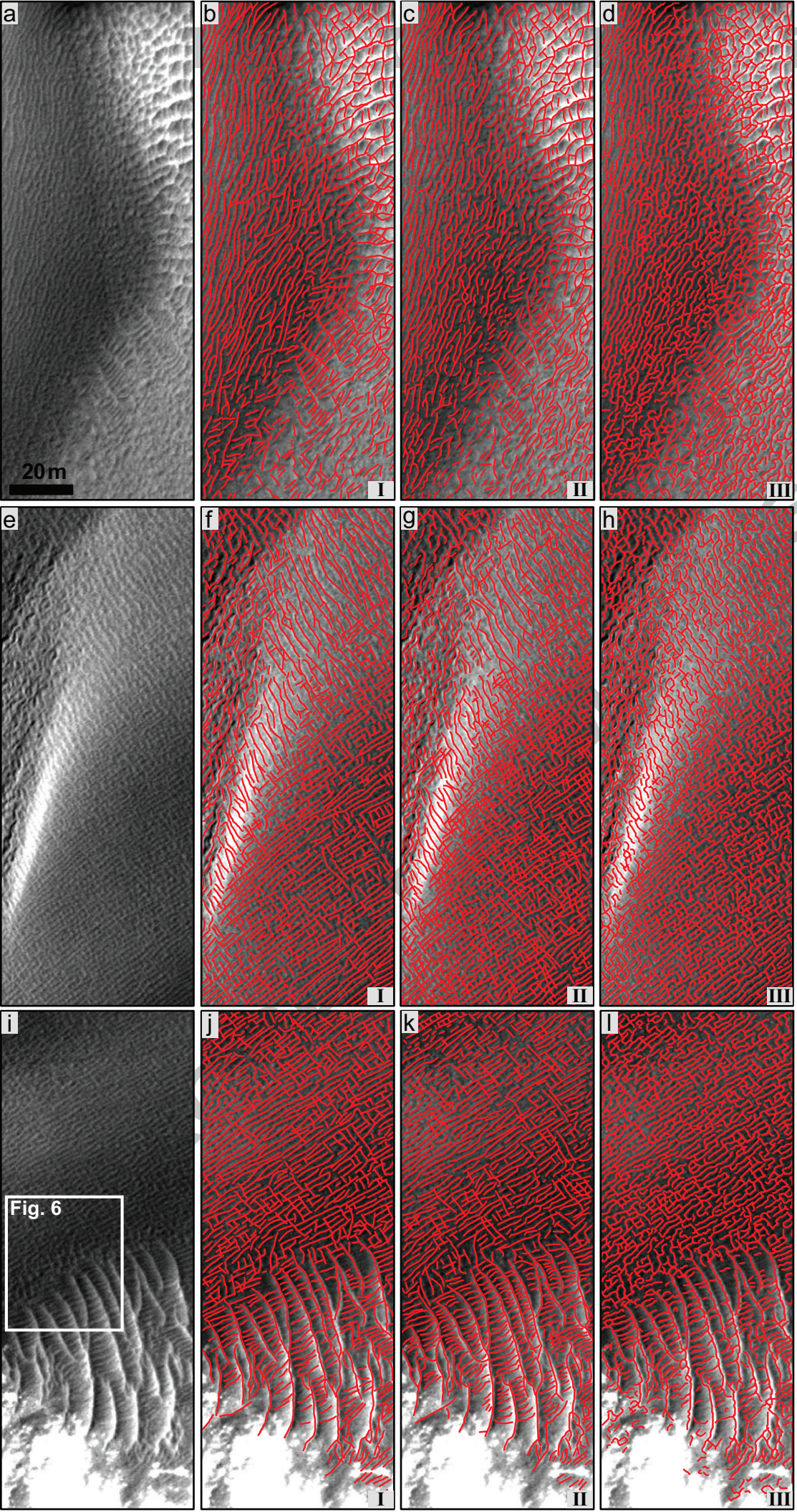
a
b
c
d
20 m
I
II
III
e
f
g
h
I
II
III
i
j
k
l
Fig. 6
I
II
III